AGU PUBLICATIONS

JGR

Journal of Geophysical Research: Space Physics

RESEARCH ARTICLE

10.1002/2016JA022432

Key Points:

- The values of afternoon Joule heating hot spot at 75 MLAT are larger in summer than in winter due to higher Pedersen conductances in summer
- The location is close to the large-scale R2/R1 FAC reversal or in some cases close to the R1/R0 reversal
- The hot spots may occur both during slow and high speed solar wind conditions and the events favor certain IMF orientations

Correspondence to:
L. Cai,
lei.cai@oulu.fi

Citation:
Cai, L., A. T. Aikio, and S. E. Milan (2016), Joule heating hot spot at high latitudes in the afternoon sector, *J. Geophys. Res. Space Physics*, *121*, 7135–7152, doi:10.1002/2016JA022432.

Received 25 JAN 2016
Accepted 22 JUN 2016
Accepted article online 4 JUL 2016
Published online 25 JUL 2016

Joule heating hot spot at high latitudes in the afternoon sector

L. Cai[1], A. T. Aikio[1], and S. E. Milan[2]

[1]Ionospheric Physics, Faculty of Science, University of Oulu, Oulu, Finland, [2]Department of Physics and Astronomy, University of Leicester, Leicester, UK

Abstract The afternoon Joule heating hot spot has been studied statistically by using the EISCAT Svalbard Radar (ESR) measurements at 75.4° Corrected Geomagnetic latitude (CGMLAT) and the OMNI solar wind data base. For a small subset of events, the Active Magnetosphere and Planetary Electrodynamics Response Experiment (AMPERE) field-aligned current distributions have been available. The main results are as follows. Afternoon Joule heating hot spots are associated with high values of ionospheric electric fields and slightly enhanced Pedersen conductances. The Joule heating hot spot values are larger in summer than in winter, which can be explained by the higher Pedersen conductances during summer than winter. The afternoon Joule heating hot spots are located close to the reversals of the large-scale field-aligned current systems. The most common location is close to the Region 1/Region 2 boundary and those events are associated with sunward convecting *F* region plasma. In a few cases, the hot spots take place close to the Region 1/Region 0 boundary and then the ionospheric plasma is convecting antisunward. The hot spots may occur both during slow (<450 km/s) and high (>450 km/s) speed solar wind conditions. During slow-speed solar wind events, the dominant interplanetary magnetic field (IMF) direction is southward, which is the general requirement for the low-latitude magnetic merging at the dayside magnetopause. During high-speed solar wind, also northward IMF conditions appear, but those are associated with large values of the IMF $|B_y|$ component, making again the dayside magnetopause merging possible. Finally, the measured afternoon hot spot Joule heating rates are not a linear function of the solar wind energy coupling function.

1. Introduction

A major part of the solar wind energy deposited in the magnetosphere-ionosphere system goes to Joule heating in the high-latitude ionosphere during geomagnetic storms, substorms, and quiet periods [e.g., *Østgaard et al.*, 2002; *Tanskanen et al.*, 2002; *Turner et al.*, 2009; *Guo et al.*, 2011; *Tenfjord and Østgaard*, 2013]. The heating represents mainly the ion-neutral frictional heating [*Vasyliūnas and Song*, 2005; *Strangeway*, 2012]. The local Joule heating causes upwelling of the neutrals, which enhances the neutral density and temperature [*Lühr et al.*, 2004], produces pressure gradients [*Kwak and Richmond*, 2007], and may excite traveling atmospheric disturbances [*Richmond*, 1978]. This heating can strongly affect the global circulation of the thermosphere. Hence, the distribution of Joule heating in the high-latitude ionosphere is one of the essential questions in the research of the coupled the magnetosphere-ionosphere-thermosphere system.

The global pattern of Joule heating has been studied by theoretical simulations [e.g., *Thayer et al.*, 1995; *Lu et al.*, 1995; *Deng and Ridley*, 2007] and empirical models [e.g., *Weimer*, 2005; *McHarg et al.*, 2005]. Those studies have revealed that Joule heating rates have maxima in two broad regions on the duskside and dawnside, which are associated with large convection electric fields within the auroral oval. Ground-based incoherent scatter radars have been used to study the statistical properties of the electromagnetic energy input and the resulting Joule heating [e.g., *Fujii et al.*, 1999; *Thayer*, 2000; *Aikio and Selkälä*, 2009; *Aikio et al.*, 2012; *Cai et al.*, 2013]. Based on the measurements by the EISCAT Tromsø radar (TRO, 66.7° CGMLAT), *Aikio et al.* [2012] and *Cai et al.* [2013] have shown that with increasing geomagnetic activity Joule heating rates increase and the evening maximum shifts to an earlier magnetic local time (MLT). *Cai et al.* [2014] (hereafter CAN14) investigated the solar wind effect on Joule heating based on the EISCAT measurements both in Tromsø and on Svalbard (EISCAT Svalbard radar, ESR, 75.4° CGMLAT). They showed that the Joule heating rates at TRO are enhanced in the evening and morning sectors for southward interplanetary magnetic field (IMF) conditions and for large solar wind electric field. Moreover, an afternoon "hot spot" in Joule heating was found by the ESR radar around 15 MLT and at 75.4° magnetic latitude, which appeared both during southward and northward IMF conditions.

The afternoon hot spot was earlier discussed in the framework of optical aurora. A bright spot was observed close to 15 MLT and 75° magnetic latitude (MLAT) [*Cogger et al.*, 1977; *Murphree et al.*, 1981]. *Moen et al.* [1994] found transient auroral arcs within 75°–76° invariant latitude and 14–15 MLT. The hot spot was also visible in a statistical study [*Liou et al.*, 1997]. It was shown that the auroral hot spot is mainly due to electron precipitation with energies less than 3 keV, and it is also associated with FACs [*Evans*, 1985; *Newell et al.*, 1996; *Kozlovsky et al.*, 2009].

To date, only a few studies have shown the afternoon hot spot in Joule heating or in the electromagnetic energy input. *Waters et al.* [2004] studied the global distribution of Poynting flux in two events during southward IMF conditions, by utilizing the magnetic field measurement by the Iridium satellites, and the electric field measurement by the Super Dual Auroral Radar Network (SuperDARN). The Poynting flux hot spot was observed in the afternoon sector at 75° CGMLAT, and it was located between an enhanced field-aligned current (FAC) pair. *Knipp et al.* [2011] investigated the Poynting flux derived from the Defense Meteorological Satellite Program (DMSP) F-15 spacecraft during 2000–2005 and found that the downward Poynting flux is often intensified in the dayside near-cusp region for the northward IMF with large B_y component. Simulations showed that the intense Poynting flux in those events was associated with an enhanced FAC pair and magnetic reconnection at the high-latitude cusps [*Li et al.*, 2011; *Wilder et al.*, 2012].

The observations of the afternoon hot spot at 75.4 CGMLAT in CAN14 were based on 39 days of data obtained by two long EISCAT Common Program 2 (CP2) experiments during 11–19 November 2003 and 1–30 September 2005. In this study, we extend the database in CAN14 by collecting all the CP2 measurements at ESR between 2000 and 2014. The larger database allows us to study the effect of the seasons, the IMF orientation, and the solar wind speed on Joule heating at 75.4° CGMLAT. In addition, we will show the relationship between the hot spot events and the local distribution of the FACs by analyzing the simultaneous observations from the Active Magnetosphere and Planetary Electrodynamics Response Experiment (AMPERE) project data during 2010–2013.

2. Measurements and Data Analysis

The EISCAT CP2 experiment is designed to have a three- or four-direction scan with high elevation angles in order to yield the electric field. At ESR (geographic: 78.15°N, 16.02°E and corrected geomagnetic: 75.43°N, 110.68°E), the 42 m antenna is fixed in the field-aligned direction and the 32 m antenna moves in a cycle of two or three positions, which results in a cycle length of 4–6 min. The measurements by the two antenna alternate so that the shorter cycle contains two 42 m antenna measurements in the field-aligned direction and two 32 m antenna measurements in two different directions and the longer cycle contains three measurements by both of the antennas. During 2000–2014, the ESR radar has in total 233 days of CP2 runs covering the MLT times in the afternoon sector.

The most probable values of the electric field with errors are estimated by the means of stochastic inversion [*Nygrén et al.*, 2011] (see more details in CAN14). The estimate is based on the assumption of a homogeneous plasma flow within the region covered by the radar beams, which corresponds to a distance of 90 km in the north-south direction and 180 km in the east-west direction. The neutral wind in the *E* region can be also estimated by using the method. However, since the analysis of the neutral wind is reliable only in some of the altitudes and MLT sectors, the neutral wind estimates are not used to calculate the Joule heating rate in this paper. The electric field is calculated at 6 min steps utilizing data over 12 min period.

In this study, we use only the field-aligned measurement by the 42 m antenna to calculate the height-integrated Pedersen and Hall conductivities. The calculation is based on the standard equations with two dominant ion species [*Brekke and Hall*, 1988; *Moen and Brekke*, 1990]. The ion-neutral and electron-neutral frequencies are calculated according to *Brekke and Hall* [1988], and the required neutral densities and temperatures are taken from the NRLMSISE-00 model [*Picone et al.*, 2002]. The actual $F_{10.7}$, $F_{10.7a}$, and *Ap* indices are used as input to the NRLMSISE-00 model. The errors of the calculated conductivities are mainly determined by the electron density measured by the ESR radar. Since the real altitude profiles of the neutral parameters are not well known, this is a source of unknown error for the conductivity altitude profiles. The height-integrated conductances are calculated by integrating the conductivity profiles from 80 km to 330 km.

The 42 m antenna stays in the field-aligned direction for about 30 s and the measurement is repeated every 1.5–2 min. During one electric field estimate six to eight conductance estimates are made and to achieve the same time resolution, the average value of the conductances is calculated. The Joule heating rate is estimated by the expression $Q_E = \Sigma_P E^2$, where Σ_P is the Pedersen conductance and E is the estimated electric field. The errors in the Joule heating rate are calculated using the estimated errors for the electric field and Pedersen conductance, which have been discussed above.

Field-aligned currents (FACs) are provided by the Active Magnetosphere and Planetary Electrodynamics Response Experiment (AMPERE) project. The project uses nearly 70 low-Earth-orbit satellites to measure the magnetic disturbance at the altitude of 780 km. The derivation of magnetic perturbations from the raw data and evaluation of the FACs from the perturbations are described by *Anderson et al.* [2000] and *Waters et al.* [2001]. The FAC maps are produced every 10 min. The AMPERE data for this study come from 2010 to 2013. During that period, we have mostly winter time CP2 runs during 21 days.

The solar wind parameters at the Earth's bow shock are provided by the OMNI database with 1 min resolution. It takes usually 1–2 min for the solar wind to travel from the bow shock to the dayside magnetopause. Typically, the global ionospheric convection responds to the solar wind conditions within 10–15 min [e.g., *Lockwood et al.*, 1986; *Ridley et al.*, 1998; *Khan and Cowley*, 1999]. In this paper, we calculated the average of solar wind parameters over a time interval starting 20 min before and ending at the time of radar measurement.

3. Statistical Results of Afternoon Hot Spots

3.1. Seasonal Variation and the Role of Electric Field and Conductivity

The seasonal effect on Joule heating at ESR is studied by organizing the data into three seasons: summer, equinox, and winter. The equinox season includes 60 days centered at the spring equinox and another 60 days centered at the autumn equinox. The summer season and the winter season include 120 days centered at the summer solstice and the winter solstice, respectively. In each season, the data are sorted in 1 h MLT bins and four IMF clock angle quadrants in the $y-z$ plane of the geocentric solar magnetospheric (GSM) coordinate system: (a) 0°–90° (B_z+/B_y+), (b) 90°–180° (B_z−/B_y+), (c) 180°–270°(B_z−/B_y−), and (d) 270°–360° (B_z+/B_y−).

Figures 1–3 show the median values of Joule heating rates at ESR for the three seasons as a function of MLT in the four IMF quadrants. The vectors indicate the plasma drift in the F region in the Earth-fixed coordinate system. The average number of samples is shown in the bottom corner of each panel. One can see that the smallest number of the measurements is made during summer. The plasma flow patterns show clear changes for different IMF conditions, as expected. The velocities are clearly larger for southward IMF conditions than for northward IMF conditions. A positive IMF B_y component produces a more round cell in the afternoon-evening sector and a negative IMF B_y produces a more crescent dusk cell. Our results are in accordance with the statistical models [see, e.g., *Pettigrew et al.*, 2010; *Cousins and Shepherd*, 2010, and reference therein].

This larger data set confirms the result by *Cai et al.* [2014] that an enhancement in Joule heating in the afternoon sector occurs statistically for all IMF quadrants. For southward IMF conditions, the maximum occurs typically at 14–15 MLT but may take place between 12 and 17 MLT. For northward IMF conditions, the maximum takes place typically somewhat later, 16–17 MLT, but may take place between 14 and 18 MLT. The Joule heating rates are larger for southward IMF conditions than for northward IMF conditions, and a clear seasonal variation can be seen as well. The winter values are smaller than during equinox or summer and therefore the color scale in Figure 3 is different from Figures 1 to 2. The summer values of the afternoon Joule heating hot spot are clearly the largest ones. One may notice that during equinox and winter, there is an enhancement in Joule heating at about 09 MLT in specific for southward IMF conditions and B_y+. At that location, the plasma flows turn toward the pole, so the enhancement may be associated with the flow channels in the morning sector during the IMF B_y positive conditions [*Sandholt and Farrugia*, 2009]. However, at the more intense afternoon hot spot the median flow directions are typically sunward. In the following, we will concentrate only on the afternoon sector.

Based on Figures 1–3, the main factors affecting the magnitude of the afternoon sector Joule heating hot spot are the IMF B_z component and the season. To quantify the typical conditions during hot spot events, we show Figure 4. We have taken all data from the afternoon sector 12–18 MLT. To find hot spot events from the data, we have set a criterion that the values of the Joule heating rate should be greater than its upper quartile for each season and IMF B_z conditions. To characterize the background conditions, we set a criterion that the

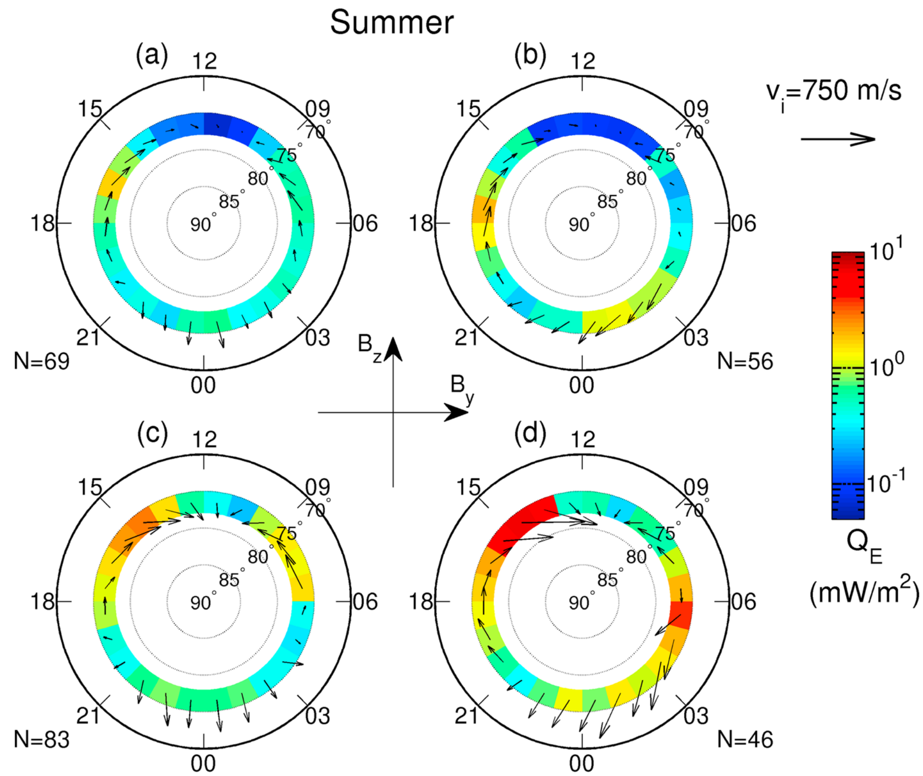

Figure 1. Median values of the Joule heating rates Q_E in the summer at ESR within 1 h MLT bins for the four IMF clock angle quadrants. The positive B_y and B_z directions are shown in the middle. The median values of *F* region plasma drift velocities are shown by vectors in each bin and the scale is indicated by the v_i vector. The average number of samples (*N*) in the bins is shown in the bottom corner of each panel.

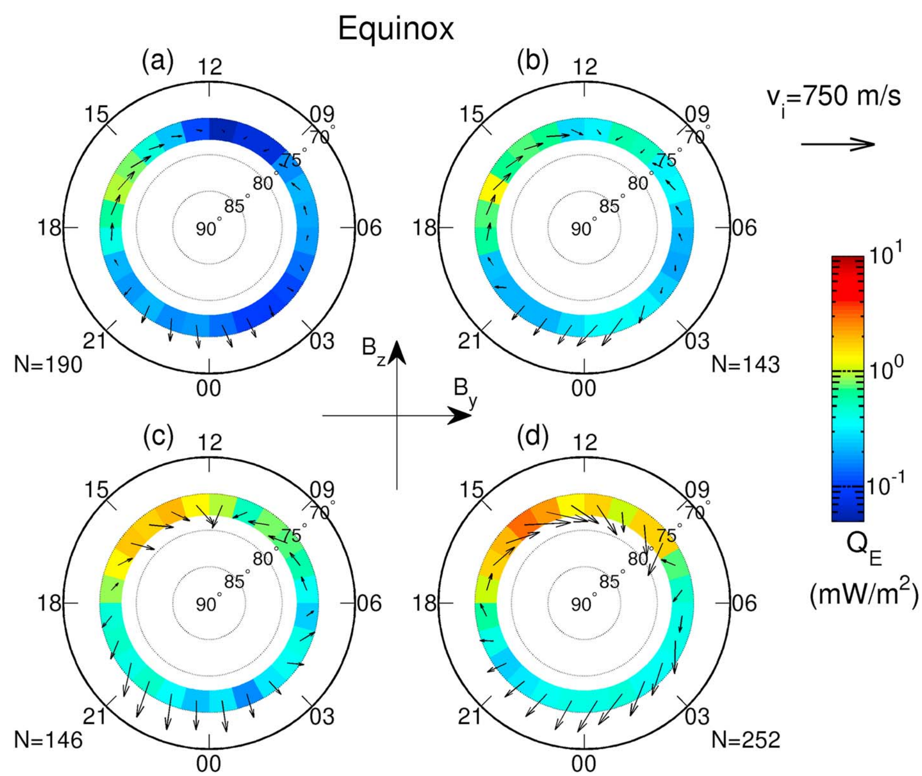

Figure 2. Median values of the Joule heating rate Q_E during equinoxes in the same format as in Figure 1.

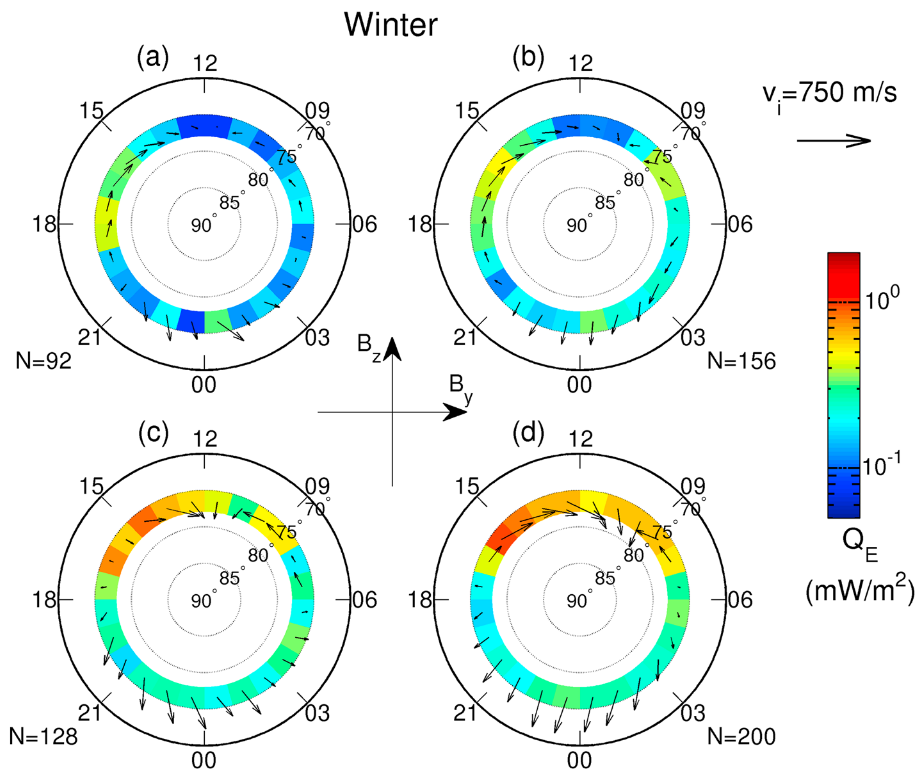

Figure 3. Median values of the Joule heating rate Q_E in the winter in the same format as in Figure 1.

Joule heating rate values should be smaller than the lower quartile for each season and IMF B_z conditions. Figure 4 (first to fourth columns) shows the median values of the electric field, its northward component, the Pedersen conductance, and the Joule heating rate for the three seasons and for northward (blue color) and southward (red color) IMF conditions. The bright color indicates hot spot events and the dark color the background events. The upper and lower quartile values are indicated by the error bars.

By definition, the Joule heating hot spots require large electric fields. For northward IMF conditions, the median values are about 28 mV/m and for southward IMF about 42 mV/m, with no significant seasonal variation. The upper quartile values during southward IMF go to about 55 mV/m. The background values are about 5 mV/m for the northward IMF and 9 mV/m for the southward IMF, which are much smaller than the hot spot values.

The large electric field for the hot spot events is mostly contributed by its northward component so that the average value is about 25 mV/m for northward IMF and about 40 mV/m for southward IMF (Figure 4, second column).

Because of the high geographic latitude, the dayside conductances on Svalbard are not large even during the summer time. The difference in Pedersen conductances for northward and southward IMF conditions during hot spot events is small but shows a seasonal variation (Figure 4, third column) with the largest values in summer (average 7.2 S), second largest during equinox (average 6.2 S), and the smallest values in winter (3.5 S). The values of Pedersen conductances are roughly in agreement with *Ridley* [2007]. The background values compared to hot spot event values are somewhat smaller during summer and equinox, but during winter the background values are only about half of the values during hot spot events. Conductances show great variability, in specific during equinox and northward IMF conditions. It is known that during northward IMF conditions cross-polar arcs may appear, which may partly explain the observations [e.g., *Kullen et al.*, 2002].

Figure 4 (fourth column) shows the Joule heating rates. During summer and southward IMF conditions, the median value for hot spots is about 9 mW/m^2 and the upper quartile value is 18 mW/m^2. Because of the seasonal change in the Pedersen conductance, both the southward and northward IMF conditions experience a similar seasonal change in hot spot Joule heating rate values with median values as follows: 3.5–8.9 mW/m^2 in the summer, 2.5–7.2 mW/m^2 in the equinox, and 1.8–3.8 mW/m^2 in the winter. The hot spot values are

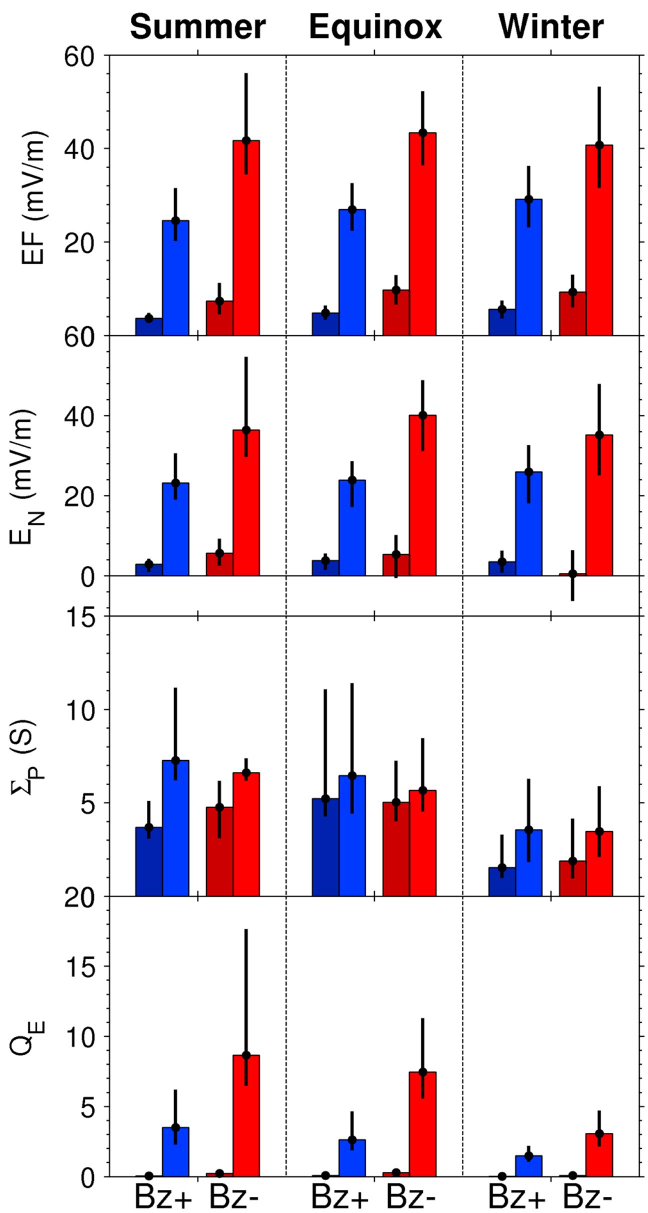

Figure 4. Median values of ionospheric parameters during afternoon Joule heating hot spots (bright bars on the right) and during background conditions (dark bars on the left) for summer, equinox, and winter seasons. Northward IMF conditions are shown in blue color and southward IMF conditions in red color. Error bars indicate the upper and lower quartile values. (first to fourth columns) The total electric field, the northward component of the electric field, the Pedersen conductance, and the Joule heating rate.

more than 2 times larger for southward IMF conditions than for northward IMF conditions in all three seasons, which is mostly caused by the larger electric field for southward IMF conditions. The background values are smaller than 0.2 mW/m^2 in all seasons due to not only the weak electric field but also the small Pedersen conductance.

3.2. Low and High Solar Wind Speed Events

Low-speed winds present the background conditions in the solar wind, whereas high values of solar wind speeds may be associated with coronal mass ejections or with high-speed stream (HSS) events originating from the coronal holes [see, e.g., *Richardson et al.*, 2000; *Tsurutani et al.*, 2006]. Our study spans both the solar cycle maximum years as well as the declining phase of the solar cycle, when the HSS events usually occur. Therefore, it is interesting to investigate if we find different characteristics for the events during these two solar wind conditions. We set the limit for slow and high speeds at 450 km/s, since it divides the data set roughly

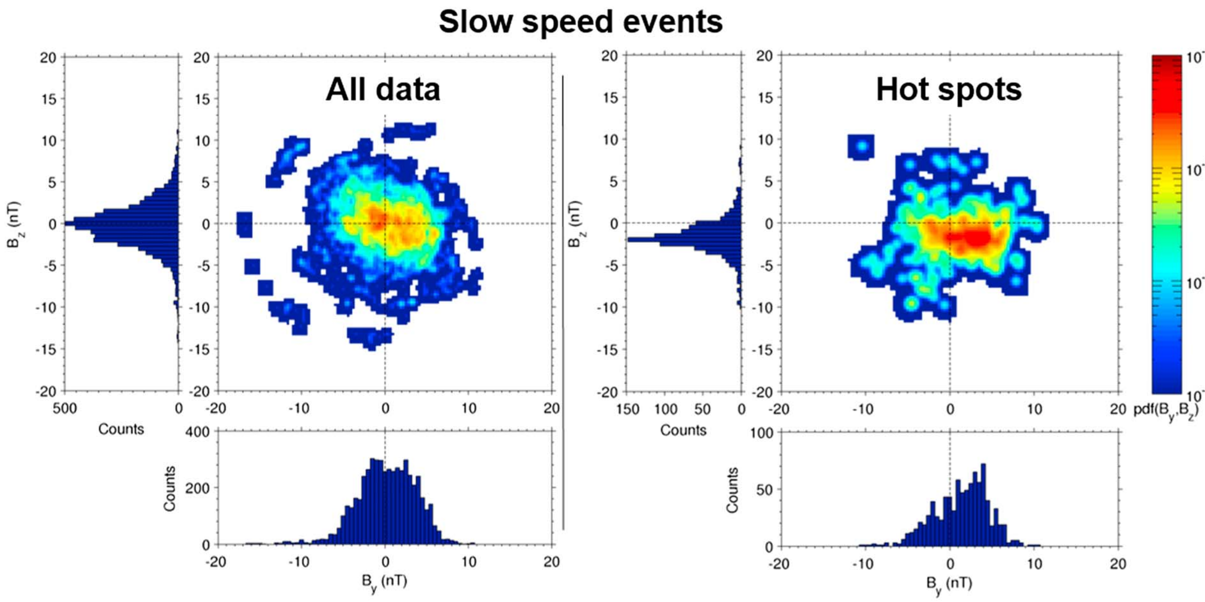

Figure 5. The two-dimensional probability density function of IMF B_y and B_z for (left) all data and the (right) hot spot events during the low solar wind speed conditions. The histograms show the marginal distribution of B_z (left) and B_y (bottom) as counts.

into two equal parts and is in accordance with values used by others [e.g., *Richardson et al.*, 2002; *Bruno and Carbone*, 2005]. Those data for which Q_E values are larger than 3 mV/m are classified as Joule heating hot spots.

Figure 5 (left) shows the two-dimensional probability density function (PDF) for IMF B_z and B_y components and for all ESR radar data utilized in this study during slow-speed solar wind conditions. We have checked that if all the IMF data during 2000–2013 would be included, the density function would be symmetric about $B_y = 0$, but since the amount of data is limited, the background data show some small asymmetries. The marginal distribution of B_z (on the left side of the left panel) is rather symmetric for positive and negative values of B_z. The marginal distribution of B_y (on the bottom side of the left panel) shows a small bias for positive values, even though there is also an enhancement in small negative values of B_y .

Figure 5 (right) displays the solar wind IMF probability density function for Joule heating hot spot events during slow solar wind speeds. The distribution of B_z has lost almost all positive (northward) values and the

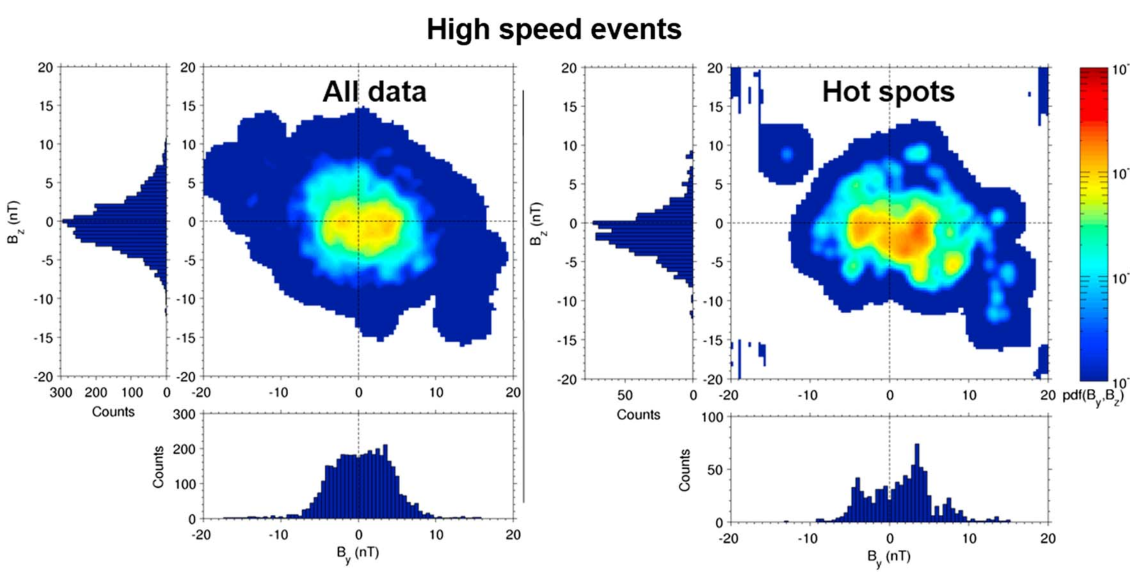

Figure 6. The probability and marginal density functions of IMF B_y and B_z during the high solar wind speed conditions in the same format as in Figure 5.

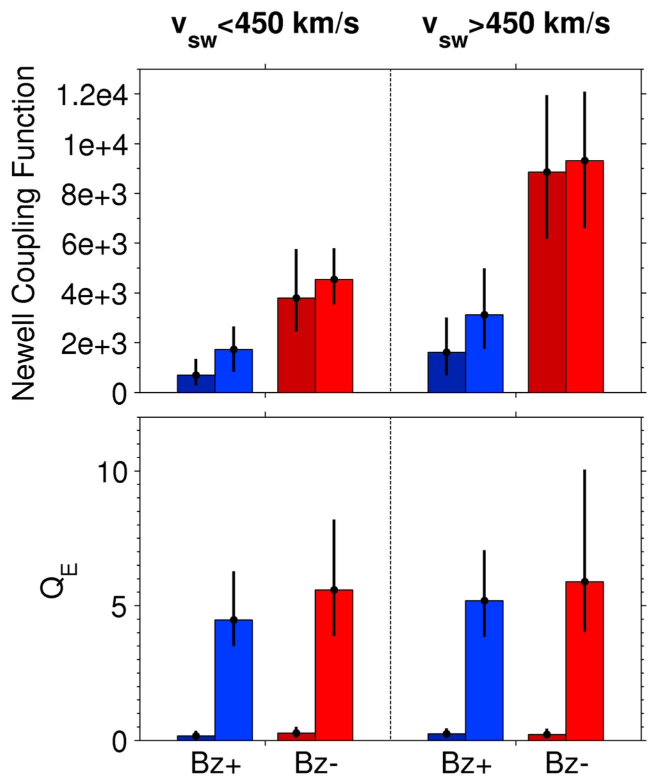

Figure 7. Median values (bars) and the lower and upper quartiles (shown as error bars) of the (top row) Newell solar wind coupling function and (bottom row) Joule heating rates for slow solar wind (left column) and fast solar wind (right column) in the same format as in Figure 4.

peak of the distribution has shifted away from zero to −2 nT. The peak of the B_y distribution is at +4 nT. The two-dimensional PDF shows clearly the dominance of southward IMF conditions and preference for positive B_y. Positive B_y produces a more round dusk cell in the convection pattern [e.g., *Ruohoniemi and Greenwald*, 2005].

Figure 6 is in the same format as Figure 5 but for high solar wind speed events. For all high-speed data (Figure 6, left), the PDF shows again some small asymmetries so that there is a bias toward B_z negative and B_y positive. The distributions are also slightly wider than for low-speed data. For Joule heating hot spot events during high-speed solar wind (Figure 6, right), the shape of B_z distribution does not change significantly compared to background conditions, meaning that hot spot events occur also during northward IMF conditions. However, the distribution of B_y experiences a drastic change so that it becomes a two-peaked function with maxima at −4 and +3.5 nT.

To further to quantify the effect of the slow- and high-speed solar wind on Joule heating hot spots we show Figure 7. Figure 7 (left column) corresponds to slow-speed solar wind conditions and Figure 7 (right column) to high-speed conditions. Figure 7 (top row) shows the Newell coupling function in the same format as Figure 4. The Newell solar wind coupling function $\mathrm{d}\Phi/\mathrm{d}t$ is a newly derived coupling function that represents the interaction between the solar wind and magnetosphere over a wide variety of magnetospheric activity [*Newell et al.*, 2007]

$$\mathrm{d}\Phi/\mathrm{d}t = v_{\mathrm{SW}}^{4/3} B_T^{2/3} \sin^{8/3}(\theta_c/2), \quad (1)$$

where v_{SW} is the solar wind speed, B_T the IMF component transverse to the GSM x direction, and θ_c the IMF clock angle in the GSM $y-z$ plane. Both for the southward (red) and northward (blue) IMF, the solar wind coupling function values are roughly double for high-speed wind compared to the slow-speed wind. This applies both for the Joule heating hot spot events (bright color) and background conditions (dark color). The values of the solar wind coupling function for southward IMF conditions are more than double compared to the northward IMF conditions, which is a natural consequence of the strong dependence of the coupling

Table 1. List of Hot Spot Events During 2010–2013 and the Associated FAC Regions (Column 3), the Direction of the Ionospheric Electric Field (E_N Northward and E_S Southward, Column 4), and the Directions of the IMF B_z and B_y Components (Column 5)

Date	Time (UT)	FACs	EF	IMF
2010-01-18	12:50–13:40	R2/R1	E_N	B_z-/B_y+
2010-01-20	13:00–13:30	R2/R1	E_N	B_z-/B_y+
2010-01-20	14:20–14:40	R1/R0	E_S	B_z-/B_y+
2010-01-21	11:45–12:10	R2/R1	E_N	B_z+/B_y+
2010-01-21	12:30–13:15	R2/R1	E_N	B_z+/B_y+
2010-01-21	13:15–14:30	R1	E_N	B_z-/B_y+
2010-01-22	12:00–13:20	R1	E_N	B_z-/B_y+
2010-01-23	11:00–13:30	R2/R1	E_N	B_z-/B_y-
2010-01-24	09:20–10:50	R2/R1	E_N	B_z-/B_y-
2010-01-24	11:40–12:40	R1	E_S	B_z-/B_y-
2010-01-25	11:00–12:40	R1	E_N	B_z-/B_y+
2011-02-04	12:10–13:00	R1	E_N	B_z+/B_y-
2011-02-05	09:10–10:40	R1/R0	E_S	B_z+/B_y-
2011-02-06	09:00–09:30	R2/R1	E_N	B_z-/B_y+
2011-02-06	09:30–12:20	R1/R0	E_S	B_z-/B_y-
2011-12-18	09:40–12:00	R2/R1	E_N	B_z-/B_y+
2012-01-13	09:30–10:40	R2/R1	E_N	B_z+/B_y+
2012-01-14	12:00–12:50	R2	E_N	B_z+/B_y+
2012-01-14	12:50–14:20	R2/R1	E_N	B_z+/B_y+
2012-01-16	10:00–11:00	R2/R1	E_N	B_z-/B_y-
2012-01-16	12:20–14:20	R1/R0	E_S	B_z-/B_y-
2012-01-17	09:40–10:50	R2/R1	E_N	B_z-/B_y-
2012-01-18	10:00–11:20	R2/R1	E_N	B_z-/B_y-
2012-01-18	12:20–14:20	R2/R1	E_N	B_z+/B_y-
2012-01-20	10:50–14:00	R2/R1	E_N	B_z-/B_y-
2013-01-10	10:00–11:30	R1	E_N	B_z-/B_y-
2013-01-11	11:00–12:30	R2/R1	E_N	B_z-/B_y+

function on the IMF clock angle. An interesting feature is that during southward IMF conditions, the difference between coupling function values during background conditions and Joule heating hot spots is small, though the median values are slightly larger during hot spots.

Figure 7 (bottom row) shows the corresponding Joule heating values. The measured median values of Joule heating for southward and, respectively, for northward IMF conditions do not change much between slow-speed and high-speed conditions, even though the solar wind coupling function values are very different. The upper quartile values for southward IMF show a slightly larger increase from slow- to high-speed events. The weak dependence of Joule heating rates on the solar wind coupling function will be discussed in section 5.

3.3. Relationship to Field-Aligned Currents

The field-aligned currents (FACs) play a central role in the energy transfer in the coupled solar wind-magnetosphere-ionosphere system. Typically, two concentric rings of current sheets can be identified in the large-scale FAC system: the poleward Region 1 (R1) current and the equatorward Region 2 (R2) current [*Iijima and Potemra*, 1978]. Region 1 currents flow into the ionosphere on the dawnside and out of the ionosphere on the duskside. Region 2 currents have an opposite polarity to Region 1 currents at a given local time sector. A pair of upward (prenoon) and downward (postnoon) currents forms poleward of R1 on the dayside during

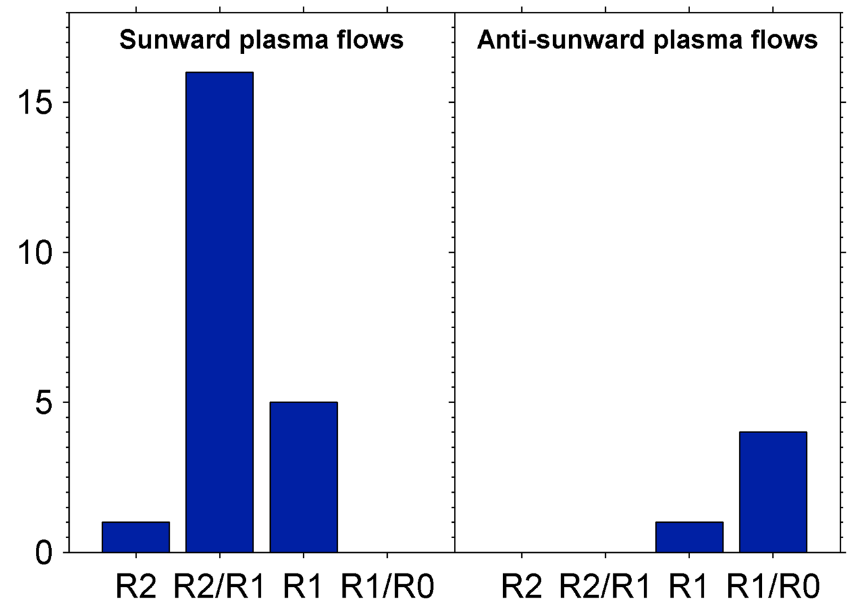

Figure 8. The number of Joule heating hot spot events from Table 1 that are associated with Region 2 current (R2), Region 2/Region 1 reversal (R2/R1), Region 1 current (R1), and Region 1/Region 0 reversal (R1/R0) for (left) sunward plasma flows and (right) antisunward plasma flows.

northward IMF [*Iijima*, 1984], but the term Region 0 currents is generally used for any currents poleward of R1 [*Ohtani et al.*, 1995; *Anderson et al.*, 2008; *Juusola et al.*, 2014].

To investigate the FACs and the convection electric field associated with the Joule heating hot spots, we listed all the hot spot events which were measured by the ESR radar in the winter during 2010–2013 in Table 1. The hot spot events were picked out according to the winter criterion used in the section 3.1.

We checked the FAC maps at the times when peaks in Joule heating rates appear during 12–18 MLT. Four types of FAC structures in the vicinity of the ESR radar were identified as follows: R2 downward current, R2/R1 reversal, R1 upward current, and R1/R0 reversal. In the afternoon sector, R0 current is downward. The FAC maps have a time resolution of 10 min, which is longer than the time interval of 6 min for the Joule heating data. We selected the FAC map at the nearest time for the Joule heating peak and listed the FAC structure types in column 3. The meridional component of the electric field at the time of the Joule heating peak is listed in column 4, which is the dominant component of the large-scale electric field in the afternoon sector as shown in Figure 4. The northward electric field (E_N) indicates a sunward plasma flow in the afternoon sector, and the southward electric field (E_s) implies an antisunward plasma flow. The corresponding IMF conditions during the hot spot events are listed in column 5. If the IMF direction fluctuates during the time interval, we give an averaged condition.

Figure 8 gives a summary of Table 1 for the relationship between the FACs and the meridional component of the electric field during the hot spot events. Of the total 27 events, 22 events were observed for sunward plasma flows (E_N) and only five events for antisunward plasma flows. For the sunward flow events, a majority of the events (73%) occur in the vicinity of the R2/R1 current reversal and 22% under the R1 current. Only one event was associated with the R2 current. For the antisunward flow events, four of the events occur in the vicinity of the R1/R0 current reversal, and one is associated with the R1 current.

The afternoon hot spot events associated with the sunward plasma flows (E_N) favor the southward IMF conditions (15 events) but appears during both B_y+ and B_y- conditions. Seven events were observed for the northward IMF but mostly with the B_y+ conditions. Events associated with the antisunward plasma flows favor the southward IMF and B_y- conditions. The preference for $Bz-$ and $By-$ for antisunward plasma flows can be explained as follows. A statistical study using the AMPERE data has shown that the Region 0 current in the postnoon sector is strongly associated with the negative B_y component [*Anderson et al.*, 2008]. Since these hot

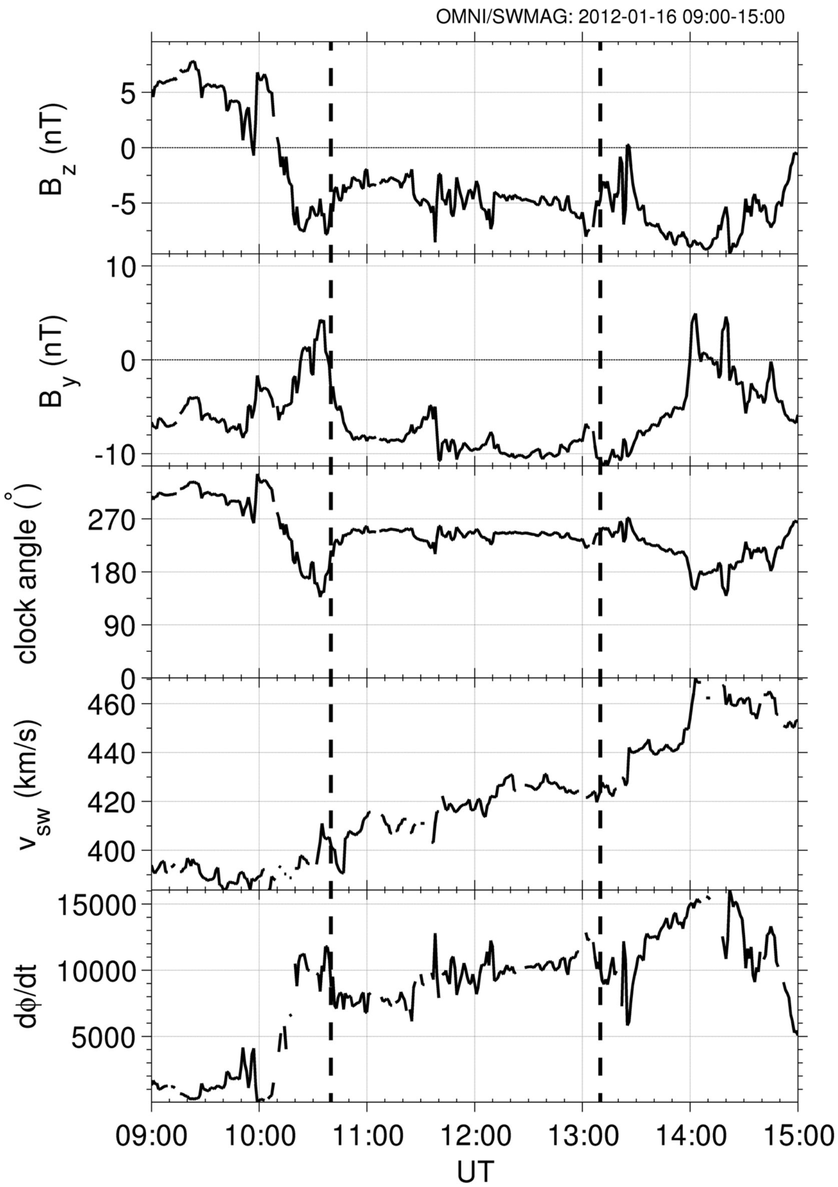

Figure 9. The solar wind and IMF parameters on 16 January 2012. (first to fifth panels) B_z, B_y, the clock angle in the GSM *y-z* plane, the solar wind speed, and the Newell solar wind coupling function.

spot events take place close to the R1/R0 current reversal, negative B_y is a natural condition. During southward IMF, the polar cap and the large-scale FAC structures expand equatorward, so it is more likely that the R1/R0 reversal moves overhead the ESR radar.

4. Afternoon Joule Heating Hot Spot Event on 16 January 2012

As Table 1 shows, many of the afternoon hot spot events occur in the vicinity of the R2/R1 large-scale current reversal. We have selected one of the events to be shown in detail here. The event on 6 January 2012 shows the typical characteristics of ionospheric parameters during the southward IMF Joule heating hot spot events in the winter time. In addition, the event takes place during strong coupling of the solar wind to the magnetosphere.

Figure 9 shows the solar wind OMNI data propagated to the dayside bow shock in the afternoon sector. At 1010 UT (MLT = UT + 3.2 h at ESR) the IMF turns southward and remains in the southward direction for the rest of the event. The B_y component is negative except during two short time intervals in the beginning and

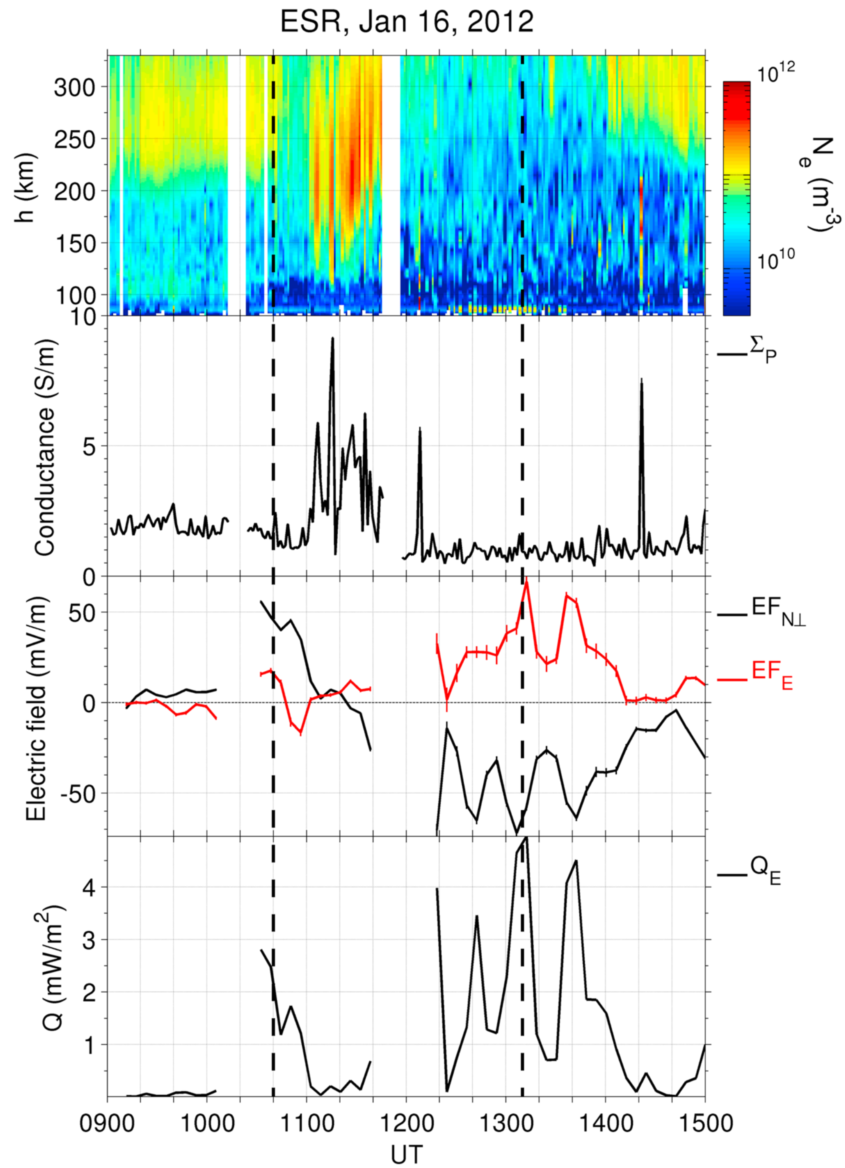

Figure 10. The ESR radar measurement of (first panel) electron density, (second panel) height-integrated Pedersen conductance, (third panel) northward (black) and eastward (red) electric fields, and (fourth panel) height-integrated Joule heating rate on 16 January 2012.

in the end of the period. B_y reaches values down to −10 nT. The IMF clock angle is around 240° for most of the time of interest (between the dashed lines). The solar wind velocity increases from 390 to 420 km/s between 10 and 13 UT, so the conditions are classified as slow speed, and only later at 14 UT the wind speed increases above 450 km/s.

After the IMF southward turning until 13 UT, the Newell coupling function varies between 8000 and 12,000. As can be seen from Figure 7, this range of the Newell coupling function values is clearly above the median for slow-speed solar wind hot spot events but within the typical range of high-speed solar wind events.

Figure 10 shows the ESR radar data. Figure 10 (first panel) shows electron densities in the *E* and lower *F* region, Figure 10 (second panel) shows the Pedersen conductance calculated from the electron density, Figure 10 (third panel) shows the northward (black) and eastward (red) electric field components, and Figure 10 (fourth panel) shows the calculated Joule heating rates. The ionospheric electric field is small until 1010 UT, after which there is a short gap in data. At 1030 UT when the IMF is already southward, the northward electric field has increased to 50 mV/m. Ionospheric conductances are rather low, but nevertheless, the Joule heating

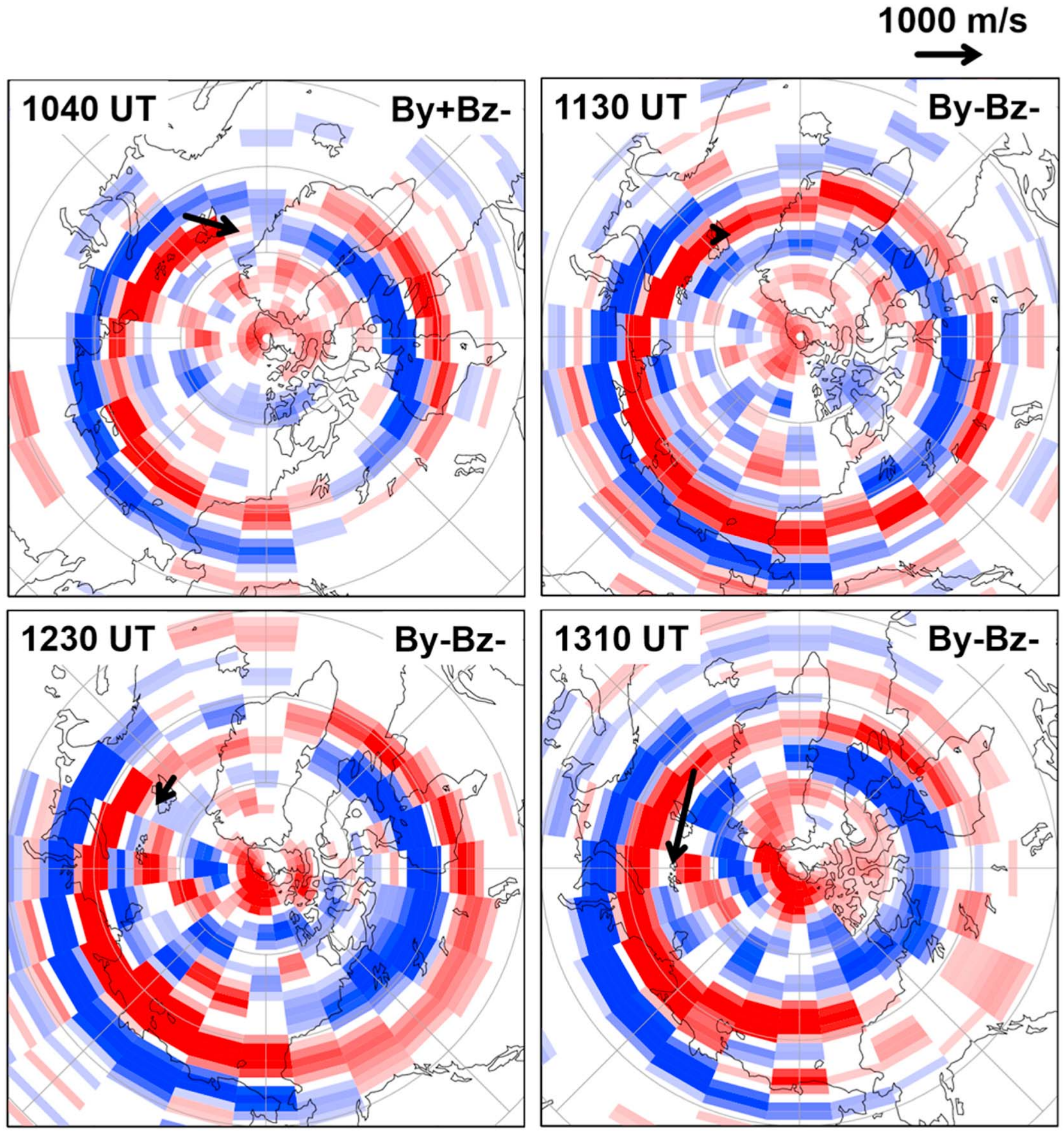

Figure 11. Selected maps of the field-aligned currents from the AMPERE project data on 16 January 2012 at (a) 1040 UT, (b) 1130 UT, (c) 1210 UT, and (d) 1310 UT. The red (blue) color indicates the upward (downward) current. The average IMF conditions during the previous 20 min are shown in the upper right corner of each panel. The *F* region plasma flow velocity measured by the ESR radar is shown by an arrow and the scale is given on the top.

rate Q_E shows a local maximum because of the high electric field values. Between 1100 and 1145 UT electron densities increase down to the *E* region indicating particle precipitation. This produces enhanced Pedersen conductances. Inside the region of higher conductances, electric field values decrease and hence also the Joule heating rates are decreased.

Figure 11 shows selected time intervals of the FAC distributions provided by the AMPERE project. Figure 11 (top left) corresponds to 1040 UT and this time has been marked by vertical dashed lines in Figures 9 and 10. At 1040 UT the IMF B_z is negative (southward) and B_y has just turned from a positive to a negative value. In our analysis, 20 min averages of the IMF before each ESR measurement are calculated. Hence, this time corresponds to IMF conditions with positive B_y. Figure 11 shows a clear pattern of downward (blue) R2 and upward (red) R1 FACs in the dusk sector. In addition, the FAC pattern has indeed the characteristics of B_y+ conditions with the duskside downward R2 connecting to the dawnside downward R1 across midday [*Anderson et al.*, 2008].

At 1040 UT, the ionospheric electric field is high in a region of low Pedersen conductance and the Joule heating rate has a local maximum. The arrow shows the *F* region plasma flow measured at ESR. The northward electric field corresponds to sunward convection and in addition the electric field has a smaller eastward component corresponding to a poleward component of the plasma flow. One can also see that the ESR radar is located in a close proximity of the R2/R1 current reversal.

At 1130 UT, the IMF B_y has been negative for 50 min and the FAC pattern has adjusted to the typical B_y- conditions with the dawnside upward R2 connecting to the duskside upward R1 across midday (Figure 11, top right). Because the dawnside downward R1 extends to the afternoon sector, three FAC sheets appear there. This extension is identified as the R0 current, since it is located poleward of the duskside R2/R1 current system. Svalbard has rotated so that it is now below the R1 upward FAC. At this time the ESR radar measures particle precipitation. As Figure 10 shows, the electric field reverses from the northward to the southward direction inside the precipitation region close to 1130 UT. Because the electric field is small, also the Joule heating rates are small.

At 1230 UT the upward R1 has expanded equatorward so that ESR is close to the poleward edge of the R1 region (Figure 11, bottom left). The electric field has turned in the southward direction, and hence, the plasma flow is antisunward. The electric field is moderate (about 35 mV/m), but the Pedersen conductance is low, so Joule heating rates are small.

At 1310 UT the ESR radar is under the R1/R0 current reversal (Figure 11, bottom right) and the plasma flows in the antisunward direction with a poleward component. The Newell solar wind coupling function during the previous 20 min has been 10,000–12,000 (the second dashed line in Figure 9 is drawn at 1310 UT). The southeastward electric field has a local maximum of 78 mV/m producing a local maximum in Joule heating rates in spite of the low Pedersen conductance.

In conclusion, in this case we find two enhanced Joule heating regions: one within the sunward flowing plasma close to the R2/R1 FAC reversal and another in the antisunward flowing plasma close to the R1/R0 FAC reversal.

5. Discussion

Figure 8 shows that the afternoon Joule heating hot spots are located close to the large-scale Region 1 field-aligned current reversals. In most cases, the location is within the sunward flowing plasma close to the equatorward boundary of the R1 current, at the R1/R2 current reversal. This result also implies that the plasma flow reversal from sunward to antisunward must take place under the afternoon sector upward R1 region. This kind of a feature is well seen also in the statistical study combining data from the CHAMP satellite and the SuperDARN radar by *Juusola et al.* [2014]. The plasma flow reversal under R1 was also visible in the individual event discussed in section 4.

In a less typical situation with the antisunward plasma flow over the ESR, the Joule heating hot spots were typically located at the poleward boundary of the R1 current, at the R1/R0 current reversal. Both under the sunward and antisunward flowing plasma, some of the events were observed under the R1 current region.

The R2 current maps to the closed field line region of the magnetosphere, whereas the mapping of R1 is more unclear. It has been suggested that the R1 current is on open field lines and connects to the magnetopause current [e.g., *Cowley*, 2013] or that R1 is partly on open field lines and partly on closed field lines [e.g., *Ohtani et al.*, 1995]. *Wing et al.* [2010] used DMSP particle data to identify the particle source populations of large-scale FACs. They found that in the afternoon sector, R2 originates from the central plasma sheet (CPS), or the boundary plasma sheet (BPS), or the inner magnetosphere, all of which are on closed field lines. The afternoon sector R1 region shows different characteristics on the equatorward and poleward part. In the whole R1 current region, BPS particles are seen, but on the equatorward part there are also CPS particles and on the poleward part the low-latitude boundary region (LLBL) particles. Because the LLBL population contains a mixture of low-energy magnetosheath-like particles and high-energy magnetospheric particles, at least part of the LLBL is likely to be on open field lines. The R0 current has BPS, LLBL, polar rain, and mantle particles of which the two latter ones clearly originate from open field lines.

The majority of the events take place within sunward convecting plasma, which obviously connects to the closed field line region of the magnetosphere. Also, the results by *Wing et al.* [2010] imply that the equatorward part of the R1 current is located on closed field lines. The antisunward flowing plasma in the afternoon sector close to the R1/R0 current reversal may map to the outer part of the LLBL, where the viscous interaction with the magnetosheath plasma produces the antisunward flow.

All the high-latitude ionospheric regions respond to the changes in solar wind driving. The strong electric fields located close to the boundaries of R1 current that we found responsible for the afternoon Joule heating hot spots are a part of the high-latitude electrodynamical system. The response of large-scale convection to various IMF conditions is rather well understood [*Ruohoniemi and Greenwald*, 2005; *Weimer*, 2005; *Cousins and Shepherd*, 2010]. The magnitude and location of large-scale FACs also respond to IMF [*Anderson et al.*, 2008; *Clausen et al.*, 2012; *Juusola et al.*, 2014]. We found that some conditions of the IMF are favored for afternoon sector Joule heating hot spots at ESR. For the slow-speed solar wind events, the favored IMF direction is southward. In addition, positive IMF B_y conditions, corresponding generally to a rounder evening cell convection, are favored. During the high-speed solar wind, both southward and northward IMF may take place. However, the northward IMF events are associated with large values of the $|B_y|$ component.

The coupling of the solar wind IMF and the terrestrial magnetosphere takes place at the dayside magnetosphere. During southward IMF, merging takes place on the low-latitude magnetopause and during northward IMF poleward of the cusps [*Dungey*, 1961]. The IMF B_y component changes the merging topology and different merging line locations are predicted by different models. However, in reality the reconnection takes place in 3-D and then one can use the concept of a magnetic separator, which is the 3-D analog of the 2-D X line [*Glocer et al.*, 2016, and references therein]. *Glocer et al.* [2016] show a simulation for the 45° IMF clock angle, which produces a tilted separator across the dayside magnetopause, and the reconnection rate has a maximum near the subsolar point. One should also note that almost all of the solar wind coupling functions depend on $\sin^n(\theta/2)$, n typically 2–4, which does not go to zero at clock angles of 90° and 270° [*Newell et al.*, 2007, and references therein]. However, when the clock angle approaches 0°, the solar wind coupling functions approach zero. Therefore, we can conclude that afternoon Joule heating hot spots are associated with dayside magnetic merging and energy input in the magnetosphere.

As the event study described in section 4 shows, local Joule heating rates may vary a lot even though the Newell solar wind coupling function remains at a high level. It is also well known that inside high-conductivity regions electric fields tend to be small [e.g., *Aikio et al.*, 2002]. So, even though enhanced dayside merging is expected to increase the global cross-polar voltage, localized variations in Joule heating rate will remain large. Our results indicate that for the ESR radar to observe afternoon Joule heating hot spot, it needs to be located close to the Region 1 current reversal, either the R1/R2 or R1/R0 reversal. This explains the poor correlation of the Newell solar wind coupling function with the locally measured Joule heating rates in Figure 7.

6. Conclusions

We have studied statistically the properties of afternoon Joule heating hot spots by utilizing the EISCAT Svalbard radar (75.4° CGMLAT) observations in the CP2 mode from 2000 to 2014 and the OMNI solar wind data base. For a subset of events, we have had the AMPERE field-aligned current distributions available. The main conclusions are as follows.

1. Afternoon Joule heating hot spots are associated with high values of ionospheric electric fields and slightly enhanced Pedersen conductances. The Joule heating hot spot values are larger in summer than in winter, which can be explained by the higher Pedersen conductances during summer than winter. The equinox values are between summer and winter. In addition, the Joule heating hot spot values are larger during southward IMF conditions than during northward IMF due to larger convection electric fields, in accordance with *Cai et al.* [2014].
2. Afternoon Joule heating hot spots are located close to the reversals of the large-scale field-aligned current systems. The most common location is close to the Region 1/Region 2 boundary and those events are associated with sunward convecting *F* region plasma (northward ionospheric electric field). In a few cases, the hot spots take place close to the Region 1/Region 0 boundary and then typically the ionospheric plasma is convecting antisunward.
3. Afternoon Joule heating hot spots may occur both during slow (<450 km/s) and high (>450 km/s) speed solar wind conditions. During slow-speed solar wind events, the dominant IMF direction is southward, which is the general requirement for the low-latitude magnetic merging at the dayside magnetopause. In addition, positive IMF B_y conditions, corresponding generally to a rounder evening cell convection, are

favored. During high-speed solar wind, the IMF B_z distribution contains both southward and northward values. The northward IMF events are associated with large values of the $|B_y|$ component, which makes again the dayside magnetopause merging possible.

4. Under the northward IMF conditions, the solar wind coupling function is clearly increased during Joule heating hot spots compared to background conditions, but under the southward IMF conditions, the increase in the solar wind coupling function is rather small compared to background conditions. The afternoon hot spot Joule heating rates are not a linear function of the solar wind energy coupling function. Obviously, an important factor affecting the measured Joule heating rates is the location of the measurement point with respect to the plasma flow and field-aligned current patterns.

There are still several open questions related to the generation of the afternoon Joule heating hot spots, such as the role of plasma velocity shears and the relationship to the afternoon auroral hot spot discovered by *Cogger et al.* [1977] and *Murphree et al.* [1981]. The spatial extent of the afternoon Joule heating hot spot is not known. If the Joule heating hot spot has a connection to the auroral hot spot, we expect the Joule heating hot spot to be located outside of the auroral hot spot, since typically plasma convection is smaller inside high-conductivity regions than outside of them [e.g., *Aikio et al.*, 2002]. In this study, we are able to observe the hot spot when it comes to the field of view of the ESR radar beam. An ideal experiment to study hot spots would contain simultaneous optical images as well as 2-D observations of plasma flows and field-aligned current distributions under known solar wind driving. Finding such an event is left for a future study.

Acknowledgments
This work was supported by the Academy of Finland (decision 285474). We thank the EISCAT Association for the incoherent scatter radar data used in this study. EISCAT is an international association supported by China (CRIRP), Finland (SA), Japan (STEL and NIPR), Germany (DFG), Norway (NFR), Sweden (VR), and United Kingdom (NERC). The EISCAT data can be obtained via the Madrigal database (http://www.eiscat.se/madrigal/). The IMF data were provided by NASA Space Physics Data Facility via OMNIWeb (http://omniweb.gsfc.nasa.gov/). We thank the AMPERE team and the AMPERE Science Center for providing the Iridium-derived data products (Contact: robin.barnes@jhuapl.edu). Analysis code used to derive the results presented in this paper is available on request from the authors. S.E.M. was supported by the Science and Technology Facilities Council (STFC), UK, grant ST/K001000/1.

References

Aikio, A. T., and A. Selkälä (2009), Statistical properties of Joule heating rate, electric field and conductances at high latitudes, *Ann. Geophys.*, *27*, 2661–2673, doi:10.5194/angeo-27-2661-2009.

Aikio, A. T., T. Lakkala, A. Kozlovsky, and P. J. S. Williams (2002), Electric fields and currents of stable drifting auroral arcs in the evening sector, *J. Geophys. Res.*, *107*(A12), 1424, doi:10.1029/2001JA009172.

Aikio, A. T., L. Cai, and T. Nygrén (2012), Statistical distribution of height-integrated energy exchange rates in the ionosphere, *J. Geophys. Res.*, *117*, A10325, doi:10.1029/2012JA018078.

Anderson, B. J., K. Takahashi, and B. A. Toth (2000), Sensing global Birkeland currents with Iridium® engineering magnetometer data, *Geophys. Res. Lett.*, *27*(24), 4045–4048.

Anderson, B. J., H. Korth, C. L. Waters, D. L. Green, and P. Stauning (2008), Statistical Birkeland current distributions from magnetic field observations by the Iridium constellation, *Ann. Geophys.*, *26*(3), 671–687, doi:10.5194/angeo-26-671-2008.

Brekke, A., and C. Hall (1988), Auroral ionospheric quiet summer time conductances, *Ann. Geophys.*, *6*, 361–375.

Bruno, R., and V. Carbone (2005), The solar wind as a turbulence laboratory, *Living Rev. Sol. Phys.*, *2*, 4, doi:10.12942/lrsp-2005-4.

Cai, L., A. T. Aikio, and T. Nygrén (2013), Height-dependent energy exchange rates in the high-latitude E region ionosphere, *J. Geophys. Res. Space Physics*, *118*, 7369–7383, doi:10.1002/2013JA019195.

Cai, L., A. T. Aikio, and T. Nygrén (2014), Solar wind effect on Joule heating in the high-latitude ionosphere, *J. Geophys. Res. Space Physics*, *119*, A020269, doi:10.1002/2014JA020269.

Clausen, L. B. N., J. B. H. Baker, J. M. Ruohoniemi, S. E. Milan, and B. J. Anderson (2012), Dynamics of the Region 1 Birkeland current oval derived from the Active Magnetosphere and Planetary Electrodynamics Response Experiment (AMPERE), *J. Geophys. Res.*, *117*, A06233, doi:10.1029/2012JA017666.

Cogger, L. L., J. S. Murphree, S. Ismail, and C. D. Anger (1977), Characteristics of dayside 5577Å and 3914Å aurora, *Geophys. Res. Lett.*, *4*, 413–416, doi:10.1029/GL004i010p00413.

Cousins, E. D. P., and S. G. Shepherd (2010), A dynamical model of high-latitude convection derived from SuperDARN plasma drift measurements, *J. Geophys. Res*, *115*, A12329, doi:10.1029/2010JA016017.

Cowley, S. W. H. (2013), Magnetosphere-ionosphere interactions: A tutorial review, in *Magnetospheric Current Systems*, edited by S.-I. Ohtani et al., pp. 91–106, AGU, Washington, D. C., doi:10.1029/GM118p0091

Deng, Y., and A. J. Ridley (2007), Possible reasons for underestimating Joule heating in global models: E field variability, spatial resolution, and vertical velocity, *J. Geophys. Res.*, *112*, A09308, doi:10.1029/2006JA012006.

Dungey, J. W. (1961), Interplanetary magnetic field and the auroral zones, *Phys. Rev. Lett.*, *6*(2), 47–48.

Evans, D. S. (1985), The characteristics of a persistent auroral arc at high latitude in the 1400 MLT sector, in *The Polar Cusp*, edited by J. A. Holtet and A. Egeland, pp. 99–109, Springer, Dordrecht, Netherlands., doi:10.1007/978-94-009-5295-9_7

Fujii, R., S. Nozawa, S. C. Buchert, and A. Brekke (1999), Statistical characteristics of electromagnetic energy transfer between the magnetosphere, the ionosphere, and the thermosphere, *J. Geophys. Res.*, *104*(A2), 2357–2365, doi:10.1029/98JA02750.

Glocer, A., J. Dorelli, G. Toth, C. M. Komar, and P. A. Cassak (2016), Separator reconnection at the magnetopause for predominantly northward and southward IMF: Techniques and results, *J. Geophys. Res. Space Physics*, *121*, 140–156, doi:10.1002/2015JA021417.

Guo, J., X. Feng, B. A. Emery, J. Zhang, C. Xiang, F. Shen, and W. Song (2011), Energy transfer during intense geomagnetic storms driven by interplanetary coronal mass ejections and their sheath regions, *J. Geophys. Res.*, *116*, A05106, doi:10.1029/2011JA016490.

Iijima, T. (1984), Field-aligned currents during northward IMF, in *Magnetospheric Currents*, edited by T. A. Potemra, pp. 115–122, AGU, Washington, D. C., doi:10.1029/GM028p0115

Iijima, T., and T. A. Potemra (1978), Large-scale characteristics of field-aligned currents associated with substorms, *J. Geophys. Res.*, *83*(A2), 599–615, doi:10.1029/JA083iA02p00599.

Juusola, L., S. E. Milan, M. Lester, A. Grocott, and S. M. Imber (2014), Interplanetary magnetic field control of the ionospheric field-aligned current and convection distributions, *J. Geophys. Res. Space Physics*, *119*, 3130–3149, doi:10.1002/2013JA019455.

Khan, H., and S. W. H. Cowley (1999), Observations of the response time of high-latitude ionospheric convection to variations in the interplanetary magnetic field using EISCAT and IMP-8 data, *Ann. Geophys.*, *17*(10), 1306–1335, doi:10.1007/s00585-999-1306-8.

Knipp, D., S. Eriksson, L. Kilcommons, G. Crowley, J. Lei, M. Hairston, and K. Drake (2011), Extreme Poynting flux in the dayside thermosphere: Examples and statistics, *Geophys. Res. Lett.*, *38*, L16102, doi:10.1029/2011GL048302.

Kozlovsky, A., T. Turunen, and S. Massetti (2009), Field-aligned currents of postnoon auroral arcs, *J. Geophys. Res.*, *114*, A03301, doi:10.1029/2008JA013666.

Kullen, A., M. Brittnacher, J. Cumnock, and L. G. Blomberg (2002), Solar wind dependence of the occurrence and motion of polar auroral arcs: A statistical study, *J. Geophys. Res.*, *107*(A11), 1362, doi:10.1029/2002JA009245.

Kwak, Y.-S., and A. D. Richmond (2007), An analysis of the momentum forcing in the high-latitude lower thermosphere, *J. Geophys. Res.*, *112*, A01306, doi:10.1029/2006JA011910.

Li, W., D. Knipp, J. Lei, and J. Raeder (2011), The relation between dayside local poynting flux enhancement and cusp reconnection, *J. Geophys. Res.*, *116*, A08301, doi:10.1029/2011JA016566.

Liou, K., P. T. Newell, C.-I. Meng, M. Brittnacher, and G. Parks (1997), Synoptic auroral distribution: A survey using Polar ultraviolet imagery, *J. Geophys. Res.*, *102*(A12), 27,197–27,205, doi:10.1029/97JA02638.

Lockwood, M., A. P. van Eyken, B. J. I. Bromage, D. M. Willis, and S. W. H. Cowley (1986), Eastward propagation of a plasma convection enhancement following a southward turning of the interplanetary magnetic field, *Geophys. Res. Lett.*, *13*(1), 72–75, doi:10.1029/GL013i001p00072.

Lu, G., A. D. Richmond, B. A. Emery, and R. G. Roble (1995), Magnetosphere-ionosphere-thermosphere coupling: Effect of neutral winds on energy transfer and field-aligned current, *J. Geophys. Res.*, *100*(A10), 19,643–19,659, doi:10.1029/95JA00766.

Lühr, H., M. Rother, W. Köhler, P. Ritter, and L. Grunwaldt (2004), Thermospheric up-welling in the cusp region: Evidence from CHAMP observations, *Geophys. Res. Lett.*, *31*, L06805, doi:10.1029/2003GL019314.

McHarg, M., F. Chun, D. Knipp, G. Lu, B. Emery, and A. Ridley (2005), High-latitude Joule heating response to IMF inputs, *J. Geophys. Res.*, *110*, A08309, doi:10.1029/2004JA010949.

Moen, J., and A. Brekke (1990), On the importance of ion composition to conductivities in the auroral ionosphere, *J. Geophys. Res.*, *95*(A7), 10,687–10,693, doi:10.1029/JA095iA07p10687.

Moen, J., P. E. Sandholt, M. Lockwood, A. Egeland, and K. Fukui (1994), Multiple, discrete arcs on sunward convecting field lines in the 14–15 MLT region, *J. Geophys. Res.*, *99*(A4), 6113–6123, doi:10.1029/93JA03344.

Murphree, J. S., L. L. Cogger, and C. D. Anger (1981), Characteristics of the instantaneous auroral oval in the 1200–1800 MLT sector, *J. Geophys. Res.*, *86*(A9), 7657–7668, doi:10.1029/JA086iA09p07657.

Newell, P. T., K. M. Lyons, and C.-I. Meng (1996), A large survey of electron acceleration events, *J. Geophys. Res.*, *101*(A2), 2599–2614, doi:10.1029/95JA03147.

Newell, P. T., T. Sotirelis, K. Liou, C.-I. Meng, and F. J. Rich (2007), A nearly universal solar wind-magnetosphere coupling function inferred from 10 magnetospheric state variables, *J. Geophys. Res.*, *112*, A01206, doi:10.1029/2006JA012015.

Nygrén, T., A. T. Aikio, R. Kuula, and M. Voiculescu (2011), Electric fields and neutral winds from monostatic incoherent scatter measurements by means of stochastic inversion, *J. Geophys. Res.*, *116*, A05305, doi:10.1029/2010JA016347.

Ohtani, S., T. A. Potemra, P. T. Newell, L. J. Zanetti, T. Iijima, M. Watanabe, M. Yamauchi, R. D. Elphinstone, O. de laBeaujardière, and L. G. Blomberg (1995), Simultaneous prenoon and postnoon observations of three field-aligned current systems from Viking and DMSP-F7, *J. Geophys. Res.*, *100*(A1), 119–136, doi:10.1029/94JA02073.

Østgaard, N., G. Germany, J. Stadsnes, and R. R. Vondrak (2002), Energy analysis of substorms based on remote sensing techniques, solar wind measurements, and geomagnetic indices, *J. Geophys. Res.*, *107*(A9), 1233, doi:10.1029/2001JA002002.

Pettigrew, E. D., S. G. Shepherd, and J. M. Ruohoniemi (2010), Climatological patterns of high-latitude convection in the Northern and Southern hemispheres: Dipole tilt dependencies and interhemispheric comparisons, *J. Geophys. Res.*, *115*, A07305, doi:10.1029/2009JA014956.

Picone, J. M., A. E. Hedin, D. P. Drob, and A. C. Aikin (2002), NRLMSISE-00 empirical model of the atmosphere: Statistical comparisons and scientific issues, *J. Geophys. Res.*, *107*(A12), 1468, doi:10.1029/2002JA009430.

Richardson, I., E. Cliver, and H. Cane (2000), Sources of geomagnetic activity over the solar cycle: Relative importance of coronal mass ejections, high-speed streams, and slow solar wind, *J. Geophys. Res.*, *105*(A8), 18,203–18,213.

Richardson, I., H. Cane, and E. Cliver (2002), Sources of geomagnetic activity during nearly three solar cycles (1972–2000), *J. Geophys. Res.*, *107*(A8), 1187, doi:10.1029/2001JA000504.

Richmond, A. D. (1978), Gravity wave generation, propagation, and dissipation in the thermosphere, *J. Geophys. Res.*, *83*(A9), 4131–4145, doi:10.1029/JA083iA09p04131.

Ridley, A. J. (2007), Effects of seasonal changes in the ionospheric conductances on magnetospheric field-aligned currents, *Geophy. Res. Lett.*, *34*, L05101, doi:10.1029/2006GL028444.

Ridley, A. J., G. Lu, C. R. Clauer, and V. O. Papitashvili (1998), A statistical study of the ionospheric convection response to changing interplanetary magnetic field conditions using the assimilative mapping of ionospheric electrodynamics technique, *J. Geophys. Res.*, *103*(A3), 4023–4039, doi:10.1029/97JA03328.

Ruohoniemi, J. M., and R. A. Greenwald (2005), Dependencies of high-latitude plasma convection: Consideration of interplanetary magnetic field, seasonal, and universal time factors in statistical patterns, *J. Geophys. Res.*, *110*, A09204, doi:10.1029/2004JA010815.

Sandholt, P. E., and C. J. Farrugia (2009), Plasma flow channels at the dawn/dusk polar cap boundaries: Momentum transfer on old open field lines and the roles of IMF B_y and conductivity gradients, *Ann. Geophys.*, *27*(4), 1527–1554, doi:10.5194/angeo-27-1527-2009.

Strangeway, R. J. (2012), The equivalence of Joule dissipation and frictional heating in the collisional ionosphere, *J. Geophys. Res.*, *117*, A02310, doi:10.1029/2011JA017302.

Tanskanen, E., T. I. Pulkkinen, H. E. J. Koskinen, and J. A. Slavin (2002), Substorm energy budget during low and high solar activity: 1997 and 1999 compared, *J. Geophys. Res.*, *107*(A6), 1086, doi:10.1029/2001JA900153.

Tenfjord, P., and N. Østgaard (2013), Energy transfer and flow in the solar wind-magnetosphere-ionosphere system: A new coupling function, *J. Geophys. Res. Space Physics*, *118*, 5659–5672, doi:10.1002/jgra.50545.

Thayer, J. P. (2000), High-latitude currents and their energy exchange with the ionosphere-thermosphere system, *J. Geophys. Res.*, *105*, 23,015–23,024, doi:10.1029/1999JA000409.

Thayer, J. P., J. F. Vickrey, R. A. Heelis, and J. B. Gary (1995), Interpretation and modeling of the high-latitude electromagnetic energy flux, *J. Geophys. Res.*, *100*(A10), 19,715–19,728, doi:10.1029/95JA01159.

Tsurutani, B. T., et al. (2006), Corotating solar wind streams and recurrent geomagnetic activity: A review, *J. Geophys. Res.*, *111*, A07S01, doi:10.1029/2005JA011273.

Turner, N. E., W. D. Cramer, S. K. Earles, and B. A. Emery (2009), Geoefficiency and energy partitioning in CIR-driven and CME-driven storms, *J. Atmos. Sol. Terr. Phys.*, *71*(10–11), 1023–1031, doi:10.1016/j.jastp.2009.02.005.

Vasyliūnas, V. M., and P. Song (2005), Meaning of ionospheric Joule heating, *J. Geophys. Res.*, *110*, A02301, doi:10.1029/2004JA010615.

Waters, C. L., B. J. Anderson, and K. Liou (2001), Estimation of global field aligned currents using the Iridium®; system magnetometer data, *Geophys. Res. Lett.*, *28*(11), 2165–2168, doi:10.1029/2000GL012725.

Waters, C. L., B. J. Anderson, R. A. Greenwald, R. J. Barnes, and J. M. Ruohoniemi (2004), High-latitude poynting flux from combined Iridium and SuperDARN data, *Ann. Geophys.*, *22*(8), 2861–2875, doi:10.5194/angeo-22-2861-2004.

Weimer, D. R. (2005), Improved ionospheric electrodynamic models and application to calculating Joule heating rates, *J. Geophys. Res.*, *110*, A05306, doi:10.1029/2004JA010884.

Wilder, F. D., G. Crowley, S. Eriksson, P. T. Newell, and M. R. Hairston (2012), Ionospheric Joule heating, fast flow channels, and magnetic field line topology for IMF By-dominant conditions: Observations and comparisons with predicted reconnection jet speeds, *J. Geophys. Res.*, *117*, A11311, doi:10.1029/2012JA017914.

Wing, S., S.-I. Ohtani, P. T. Newell, T. Higuchi, G. Ueno, and J. M. Weygand (2010), Dayside field-aligned current source regions, *J. Geophys. Res.*, *115*, A12215, doi:10.1029/2010JA015837.